ACS OMEGA

http://pubs.acs.org/journal/acsodf

Article

Scalable Hybrid Antibacterial Surfaces: TiO_2 Nanoparticles with Black Silicon

Jagriti Singh,* Prajwal B. Hegde, Sushobhan Avasthi, and Prosenjit Sen

Cite This: *ACS Omega* 2022, 7, 7816−7824

Read Online

ACCESS | Metrics & More | Article Recommendations

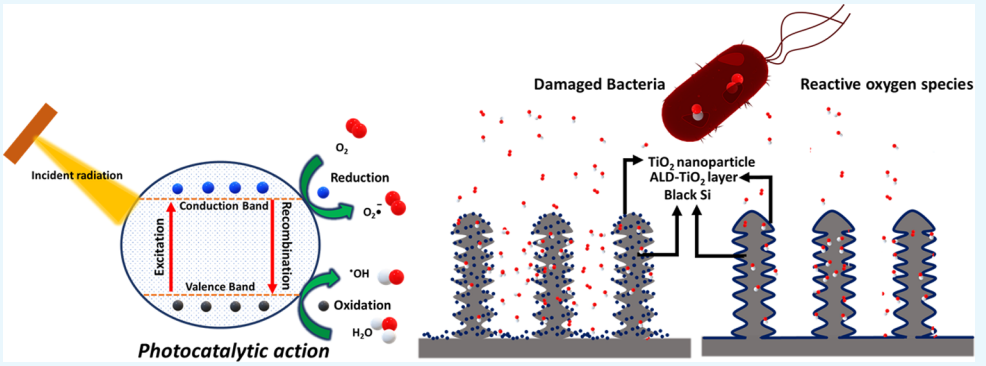

ABSTRACT: With the increase of drug resistance, there is a need for surface coatings that inhibit microbes without antibiotics. Nanostructured photocatalysts, like TiO_2-coated nanotubes, are promising alternatives to antibiotics. Nanostructures rupture the cell wall by impaling the bacteria. Photocatalysts generate reactive oxygen species (ROS) in the presence of light, which oxidize organic matter. The combined effect of photocatalysts and nanostructures is better than the addition of individual components, as nanostructures also enhance the ROS production by trapping light. The synergetic effect is remarkably effective in reducing the growth of bacterial colonies, but scalability still remains a challenge. Conventional techniques like atomic layer deposition (ALD) are excellent for proof of concept but are not scalable to hundreds of square meters, as needed for practical applications. This report demonstrates two scalable and cost-effective techniques for synthesizing photocatalytic nanostructures: spray- and spin-coating TiO_2 nanoparticles. Unlike ALD, spray- and spin-coated TiO_2 nanoparticles do not reduce the roughness of a structured surface, which improves antibacterial performance by 23%. Integration of nanostructures with spray-coated TiO_2 is potentially a low-cost and scalable technology for large-area antibacterial surfaces.

1. INTRODUCTION

The invention of antibiotics is one of the great success stories of modern medicine. Unfortunately, bacteria evolve much faster than the rate at which we can develop new antibiotics. Antimicrobial resistance (AMR) may cause 10 million deaths per year by 2050, costing $100 trillion by 2050.[1−4] AMR often starts with bacterial colonization on high-touch surfaces, e.g., in hospitals, catheters, stethoscopes, surgical tools, etc.[5] If not contained in the initial stage, bacteria colonies grow to form biofilms that are very hard to eradicate. AMR breeds in these biofilms. The best way to reduce AMR is to inhibit the initial attachment of bacteria to high-touch surfaces using antibacterial coatings.

Antibacterial materials used today can be broadly classified into organic and inorganic biomaterials. The antibacterial action of metal ions such as silver, copper, cobalt, zinc, zirconium, gold, etc.,[6,7] is caused due to their intracellular accumulation across cell membrane disrupting bacteria.[6] Inorganic nanoparticles such as calcium phosphate, silver, copper, gold, zinc, aluminum oxide, copper oxide, and magnesium oxide exhibit antibacterial efficacy through multiple pathways, which include cell wall penetration, ROS production, gene modification, and metabolite binding.[8] Even though inorganic biomaterials are broad-spectrum biocides and thermally and chemically stable, their bioaccumulation and toxicity have a wider implication in their applications. These issues can be overcome using organic materials like polyethylenimine containing quaternary ammonium groups, nanofibrillated cellulose/chitosan nanoparticles, polyaniline/poly(3-aminobenzoic acid), polypyrrole, etc.[9−12] Their antibacterial mechanism is localized in action resulting in

Received: November 27, 2021
Accepted: January 14, 2022
Published: February 25, 2022

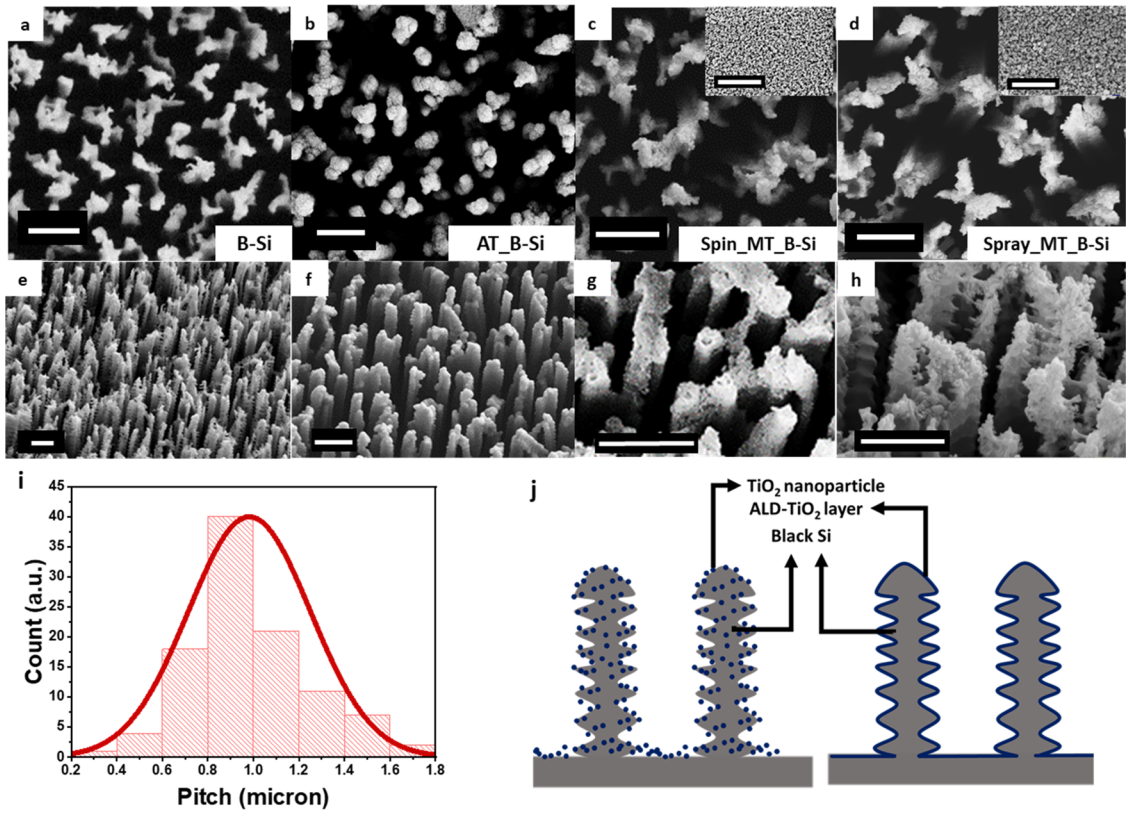

Figure 1. Scanning electron microscopy images of surfaces. Top view scanning electron microscopy (SEM) images of (a) B-Si and (b) ALD-coated B-Si (AT_B-Si).[40] Mesoporous nanoparticles (c) spin-coated (Spin_MT_B-Si) and (d) spray-coated (Spray_MT_B-Si) on B-Si. 45° view SEM images of (e) B-Si and (f) ALD-coated B-Si (AT_B-Si). Mesoporous nanoparticles (g) spin-coated (Spin_MT_B-Si) (h) spray-coated (Spray_MT_B-Si) on B-Si. Scale bar: 1 μm (i) Distribution of pitch (center-to-center spacing) of black Si. (j) Schematic representation of nanoparticle-coated black Si versus ALD-coated B-Si.

organelle disturbance and disruption of the intercellular biochemical pathway.[13] In recent studies, it has been shown that some of the carbon-based materials such as graphene oxide, nanodiamonds, fullerene 60 nanoparticles, and carbon nitride nanomaterials are also biocides.[14−17]

In recent decades, new antibacterial mechanisms are experimented with to combat antibacterial resistance. These include microwaveocaloric, sonodynamic therapy, and photoresponsive therapy.[18,19] Photoresponsive materials are light-activated materials, which absorb light to kill bacteria.[20−22] Photocatalysts such as ZnO and TiO_2 kill bacteria via reactive oxygen species (ROS) produced under sub-band-gap illumination. In this report, we have utilized TiO_2 as an antibacterial photocatalytic material. The band gap of anatase TiO_2 is 3.2 eV, so under 365 nm UV light, an electron−hole pair is created in TiO_2 that reacts with water and oxygen to form ROS. The ROS decompose organic matter, killing the bacteria. Photocatalytic efficacy is extremely sensitive to the active surface area, the thickness of TiO_2, and the diffusion length of carriers. Unfortunately, TiO_2 thin films are deficient in all three. The effective surface area of TiO_2 thin films is limited. The absorption depth of UVA radiation (365 nm) in TiO_2 is ∼1 μm, so absorbance in a 100 nm film is less than 10%. The photogenerated charge carriers must diffuse to the surface to generate ROS. For anatase, the diffusion length is only 5 nm,[23] so the efficiency of photon-to-ROS conversion in a 100 nm film is only ∼0.04.[24]

Recently, the Ivanova group found nanostructured antibacterial surfaces on Cicada wings[25] that is a mechanical way of killing bacteria without the involvement of any chemical compound. Nanostructures kill the bacteria by impaling and rupturing the cell wall. Researchers have now observed them on dragonfly wings, gecko skin, shark skin, etc. Artificial nanostructured surfaces have also been developed, e.g., PMMA films,[26] structured polystyrene surfaces,[27] Au nanostructured surfaces,[28] black silicon, and black titanium.[29,30]

It has been observed that a synergetic combination of various individual mechanisms can enhance antibacterial efficacy. For instance, graphene oxide[31,32] in combination with several metal compounds, hybrid coatings of polydopamine/Ag_3PO_4/graphene oxide and CuS/graphene oxide, hybrid metal−organic frameworks[33,34] of Prussian blue and PCN-224, red phosphorous[35,36] combining photothermal and photocatalytic effects, etc., exhibits enhanced antibacterial activity compared to single systems.[37−39]

Recently, we combined photocatalytic TiO_2 films with nanostructures to obtain superior antibacterial performance. The addition of nanostructures ameliorates the intrinsic limitations of photocatalyst films like TiO_2. Nanostructures enhance light absorption in TiO_2 by scattering photons, which increases the effective path length of light through the film. Nanostructures also increase the active surface area, leading to higher production of ROS and lower bacterial counts.[40] Black silicon (B-Si) coated with the TiO_2 photocatalyst is more effective than either B-Si or TiO_2.

Bacterial colonies are most common on multiuse medical equipment, like surgical tools,[41] tubings,[42] catheters,[43] and frequently touched surfaces, such as door handles[44] and tables.

https://doi.org/10.1021/acsomega.1c06706
ACS Omega 2022, 7, 7816−7824

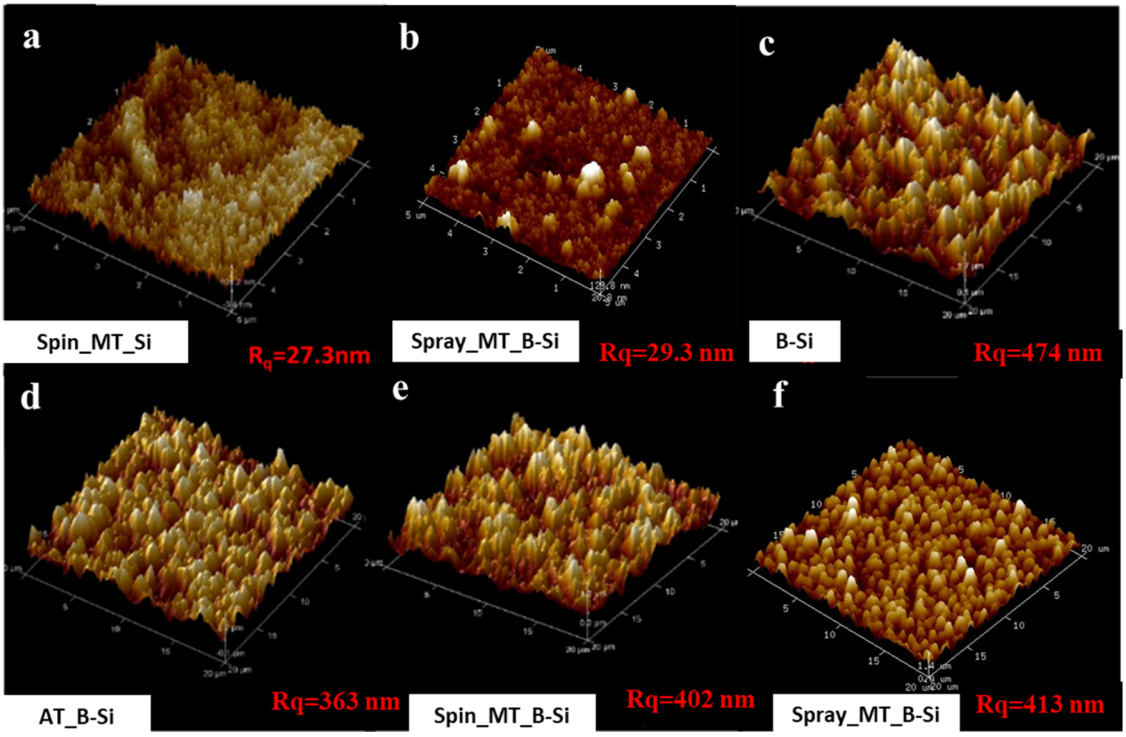

Figure 2. Atomic force microscopy 3D images of (a) spin-coated mesoporous TiO_2, (b) spray-coated mesoporous TiO_2, (c) black silicon, (d) ALD-deposited TiO_2 on black silicon, (e) mesoporous TiO_2 spin-coated on black Si, and (f) mesoporous TiO_2 spray-coated on black Si. The surface roughness is highest in B-Si. It reduces on TiO_2-coated surfaces. The R_q value indicates the root mean square roughness of surfaces.

Even in a modest hospital, the cumulative area of all such surfaces is several hundred square meters.[45] Any practical antibacterial solution must be cost-effective at this scale. Chemical vapor deposition (CVD) is commonly used to deposit functional nanofilms. Unfortunately, CVD equipment is complex. Precursors are toxic, explosive, and corrosive, so they require special handling.[46] Atomic layer deposition (ALD) is the most common form of CVD for metal oxides due to its excellent repeatability, control, film quality, structural conformity, and adhesion. But the economic viability of ALD over vast areas is questionable due to low deposition rates and high wastage of expensive precursors.[47] Physical vapor deposition (PVD), such as thermal evaporation, e-beam evaporation, and sputtering, is more straightforward and low-cost. However, the film quality is inferior, nonuniform, and nonconformal. In addition, objects with complex curves cannot be coated uniformly in three dimensions (3D) with low-cost PVD.

In our recent work on nanostructured photocatalysts, we showed that TiO_2-coated nanopillars have the best bactericidal properties.[40] The TiO_2 layer was deposited via atomic layer deposition (ALD). For scalability, it is desirable to explore other low-cost scalable deposition techniques.[48] A technique is recently developed to transfer copper nanowires onto a curable silicon PDMS structure through the mechanical tearing process.[49] An electrochemical additive manufacturing technique was introduced to fabricate fluoridated hydroxyapatite nanostructures.[50] A single-step replication process through UV-curable polymers to fabricate a transferable flexible nanostructure array is also developed.[51] Combining these techniques with inexpensive spin or spray coating would bring down the cost of production for commercial application.[52,53]

This work shows that nanostructured photocatalysts can be improved further by depositing the photocatalysts as a nanoparticle instead of a thin film. The process is significantly cheaper and more scalable than ALD because the nanoparticles are deposited by spin and spray coating. The bactericidal efficacy of B-Si is better with printed TiO_2 nanoparticles than the TiO_2 thin film. The sharp nanoparticles also cause mechanical damage to bacteria.[40,54] The effective surface area of the photocatalyst is significantly larger, which boosts the production of ROS. The quantum efficiency of photon-to-ROS conversion is better because photogenerated carriers in TiO_2 are always within the diffusion length of the surface.

2. RESULTS AND DISCUSSION

The B-Si described here has a forest of vertical nanostructures (Figure 1i), whose fabrication method has been reported earlier in our previous work.[40] The center-to-center distance between pillars follows a Gaussian distribution with a mean of 1 μm. B-Si was coated with TiO_2 using three different methods: atomic layer deposition (AT_B-Si), spin coating (Spin-MT_B-Si), and spray coating (Spray-MT_B-Si). ALD yields a conformal and continuous thin film (50 nm TiO_2), while spin and spray coating yield a mesoporous film. Figure 1a–h shows the SEM of the resulting surfaces, and Figure 1j shows the schematic difference between black Si coated with mesoporous TiO_2 and black Si coated with ALD TiO_2.

B-Si has an RMS roughness of ~474 nm. With ALD TiO_2 coating on top of it, the roughness decreases to 363 nm because the conformal TiO_2 film reduces the sharpness of the nanopillars. The mesoporous coating consists of 25 nm (diameter) TiO_2 nanoparticles. The nanoparticles cover the surface of B-Si uniformly. The RMS roughness of flat silicon surfaces with spray- and spin-coated TiO_2 nanoparticles is of the same order as the particle size, i.e., 27 and 29 nm, respectively. The RMS roughness of Spin-MT_B-Si and Spray-MT_B-Si is

https://doi.org/10.1021/acsomega.1c06706
ACS Omega 2022, 7, 7816−7824

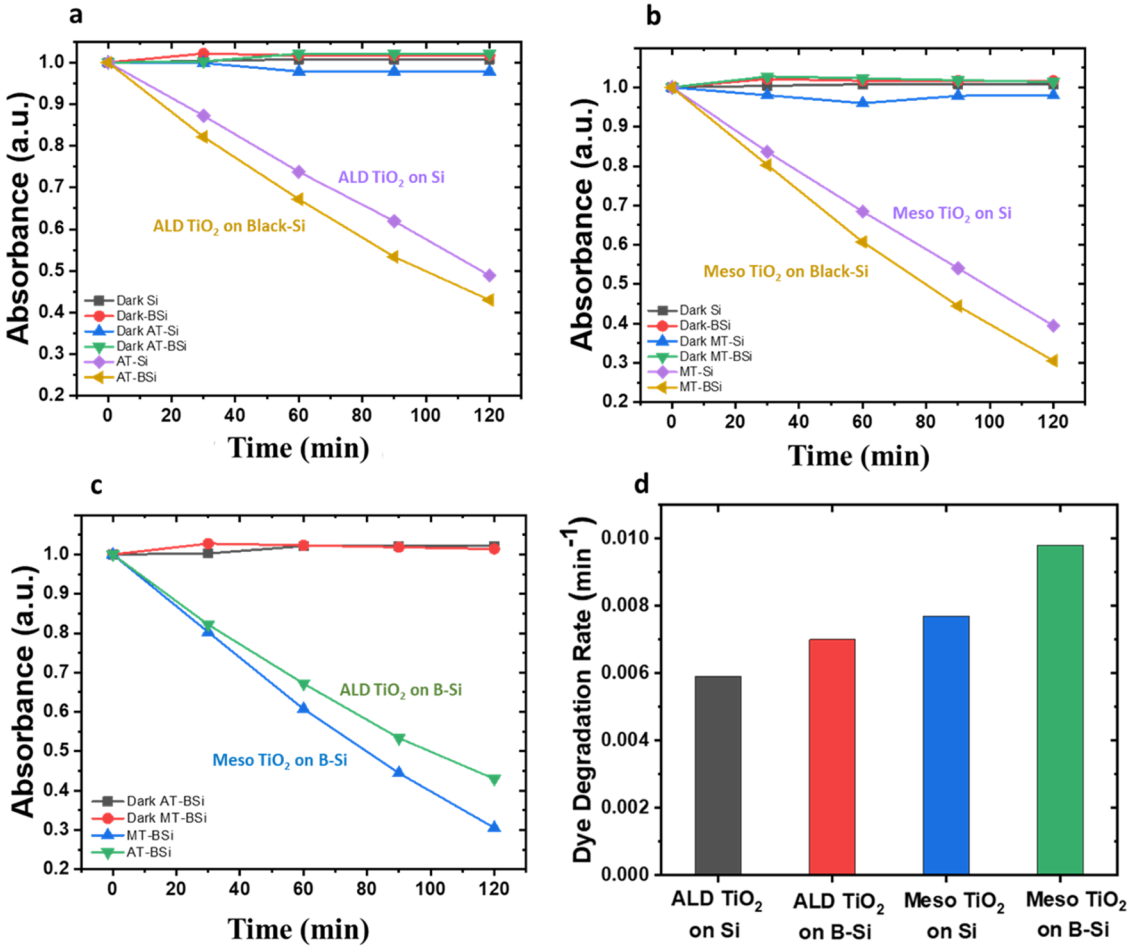

Figure 3. Methylene blue dye degradation of different surfaces in the presence of UV-365 nm. (a, b) Enhanced performance of TiO_2-coated B-Si (AT_B-Si, MT_B-Si) over a flat surface. (c) Comparison of mesoporous and ALD TiO_2 coatings indicates that mesoporous TiO_2 performs better. (d) Comparison of the methylene blue dye degradation rate on different surfaces.

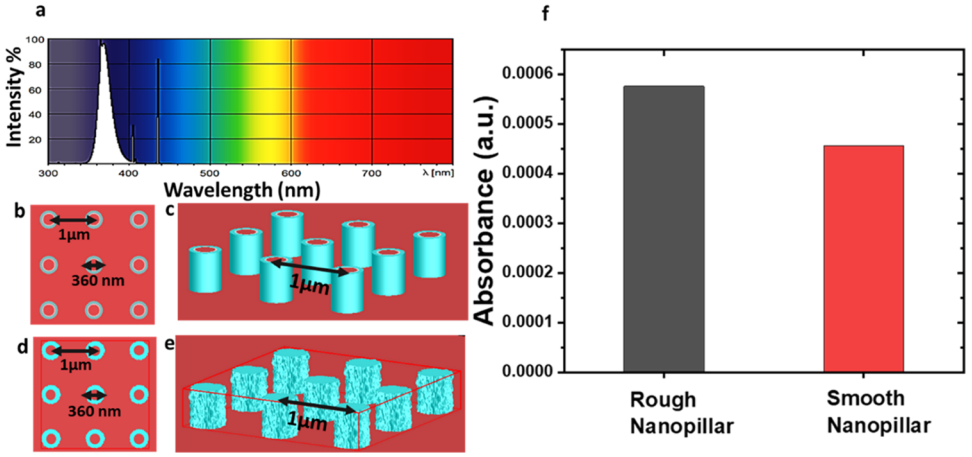

Figure 4. (a) Wavelength versus intensity percentage spectra of the UV source used in all experiments. (b–e) System of the pillar array used in FDTD simulations mimicking TiO_2-coated B-Si: (b) top view and (c) tilted view of the smooth TiO_2 coating on Si pillars. (d) Top view and (e) tilted view of the rough TiO_2 coating on Si pillars. (f) Absorbance of light in the TiO_2 layer of the rough versus smooth system of the nanopillar array.

~400 nm, similar to that of B-Si (Figure 2). The nanopillars retain their sharpness when coated with mesoporous TiO_2.

ROS generation was quantified using methylene blue (MB) dye under a UVA illumination of 19 W/m^2. Reactive oxygen species produced by TiO_2 bleach the MB dye. The bleaching rate is modeled as follows

$$k = \frac{1}{t} \ln\left(\frac{C_o}{C}\right)$$

C is the concentration observed at t min, and C_o is the initial concentration of the dye. Measurements were made for the three nanostructured photoactive films: ALD TiO_2-coated black

https://doi.org/10.1021/acsomega.1c06706
ACS Omega 2022, 7, 7816−7824

silicon (AT_B-Si), spin-coated mesoporous TiO_2 on black Si (Spin-MT_B-Si), and spray-coated mesoporous TiO_2 on black Si (Spray-MT_B-Si). As a control, experiments were also performed on flat silicon surfaces: ALD TiO_2 on Si (AT_Si), spin-coated mesoporous TiO_2 on Si (Spin-MT_Si), and spray-coated mesoporous TiO_2 on Si (Spray-MT_Si) (Figure 3a–c). As reported previously, nanostructuring increases ROS production in TiO_2: the MB degradation rate increased from 0.0059 min^{-1} for AT_Si to 0.0070 min^{-1} for AT_B-Si. A similar effect is also seen for mesoporous TiO_2: the MB degradation rate increased from 0.0077 min^{-1} for MT_Si to 0.0098 min^{-1} for MT_B-Si (Figure 3d). In addition, the nanostructures increase the light absorption in TiO_2 and the effective surface area of the photocatalyst. Both of which lead to higher ROS generation and dye degradation rates.

The nanostructures improve the absorption of light due to light trapping. Conformal ALD reduces the sharpness of the B-Si nanopillars, but mesoporous coatings do not. So the dye degradation rate on MT_B-Si (0.098 min^{-1}) is higher than that on AT_B-Si (0.007 min^{-1}). Ray optics cannot model the interaction of light with the nanopillar array due to subwavelength features. We used the finite-difference time-domain (FDTD) method to calculate the first-principle solution of Maxwell's equation using Lumerical. The nanopillars are modeled as a two-dimensional cylindrical array with a radius of 130 nm and a center-to-center distance of 1 μm, matching the dimensions of B-Si. The light source is 365 nm, matching the peak wavelength of light used in the experiments (see Figure 4a). The electromagnetic field has a plane of symmetry through the middle of the simulated region, so we use symmetric and antisymmetric boundary conditions. We model the substrate at the bottom of the array as a perfectly matched layer (PML), i.e., a perfect absorber. The Experimental Details section contains the FDTD parameters of the TiO_2-coated nanopillar simulation. The B-Si nanopillars trap light. The nanopillars with the conformal ALD TiO_2 layer perform similarly. The nanopillars coated with mesoporous TiO_2 have a higher RMS roughness of ~25 nm (typical diameter of the nanoparticles). This improves light trapping, which leads to higher absorption in the TiO_2 layer, increased ROS, and, as we shall show later, a higher antibacterial effect.

We use *Escherichia coli ATCC 25922* to test the surfaces for bactericidal activity. The CFU count shows the number of viable bacteria on a surface. The lower the CFU count, the better the bactericide. The UVA illumination intensity used in experiments was 19 W/m^2, which is comparable to the UVA component present in sunlight [4]. Nanostructured B-Si is better than planar Si for all of the TiO_2 coatings: ALD (AT_B-Si), spin-coated (Spin MT_B-Si), and spray-coated (Spray MT_B-Si, Figure 5). Compared to the planar surface, the bacterial count on B-Si decreases by 61% with the ALD TiO_2 coating and 70% for the mesoporous TiO_2 layer (Figure 5). The results prove that nanostructures improve the bactericidal efficiency of TiO_2 coatings.

Scanning electron microscopy images in Figure 6 show the changed morphology of bacteria on TiO_2 surfaces compared to the control flat silicon surface. The flat and ALD-coated images have been derived from our previous work, with the addition of spray- and spin-coated surfaces.[40] In Figure 6, the blue arrow indicates the piercing of bacteria by the pillars. The red arrow indicates damaged cell wall areas. The yellow arrow indicates sunken bacteria. Figure 6a indicates undamaged bacteria on flat silicon. Figure 6b–d shows bacterial cell wall disruption on TiO_2 surfaces. Figure 6e shows that the pointed structures of B-Si impale the bacteria. Figure 6f–h shows that bacteria have sunken inside the TiO_2-coated pillars, indicating cell death.

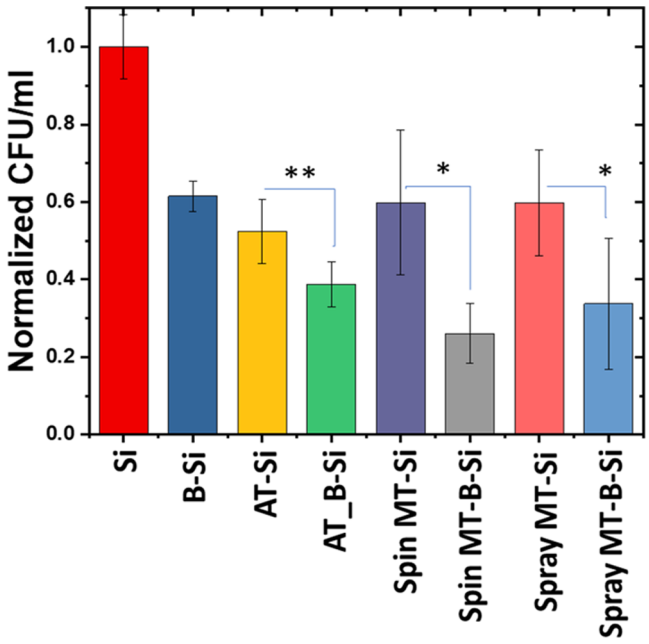

Figure 5. Normalized CFU count comparison of different surfaces. The bacterial count reduces by 38% due to the nanopillar's mechanical killing effect on B-Si. The photocatalytic effect integrated with mechanical bactericidal reduces the bacterial count by 30% in B-Si-coated TiO_2 surfaces (AT_B-Si) compared to flat TiO_2 surfaces (AT_Si).

Mesoporous TiO_2 performs better than ALD TiO_2. The CFU count on B-Si with mesoporous TiO_2 is 23% lower than B-Si with ALD TiO_2. This corroborates the MB degradation studies, which show that B-Si with mesoporous TiO_2 degrades 40% more dye than B-Si with ALD TiO_2.

3. CONCLUSIONS

We demonstrated that the introduction of nanostructures improves the antibacterial activity of photocatalytic TiO_2 coatings. The rough grass-like structures on B-Si increase the active surface area of TiO_2, boosting the photon-to-ROS conversion efficiency. Also, the light falling on the high-aspect-ratio nanostructure gets trapped, increasing light absorption. The performance and cost-effectiveness can be further improved by replacing the TiO_2 thin film with a mesoporous TiO_2 layer. We can deposit mesoporous TiO_2 by spin or spray coating, a drastically more scalable and low-cost process than ALD.[49−51] The nanoparticles of TiO_2 are even better at converting photons to ROS. Also, the sharp features of nanoparticles cause damage to bacteria.[40,54] Under UVA illumination, nanostructured photocatalysts are 60–70% better at killing bacteria than flat photocatalysts. Also, the bactericidal activity of nanostructured black Si is 23% higher with mesoporous TiO_2 than the TiO_2 thin film. These results further highlight the importance of nanoscale topological roughness in antibacterial activity, providing a path for scalable, low-cost, and large-area antibacterial surfaces.

4. EXPERIMENTAL DETAILS

4.1. Fabrication of a Dual-Action Surface. Silicon chips of 2 × 2 cm^2 (n-type, ⟨100⟩, 1−100 Ω cm-1, 450 μm) were piranha-cleaned (in a solution of 1:3 H_2SO_4 and H_2O_2 for 10

https://doi.org/10.1021/acsomega.1c06706
ACS Omega 2022, 7, 7816−7824

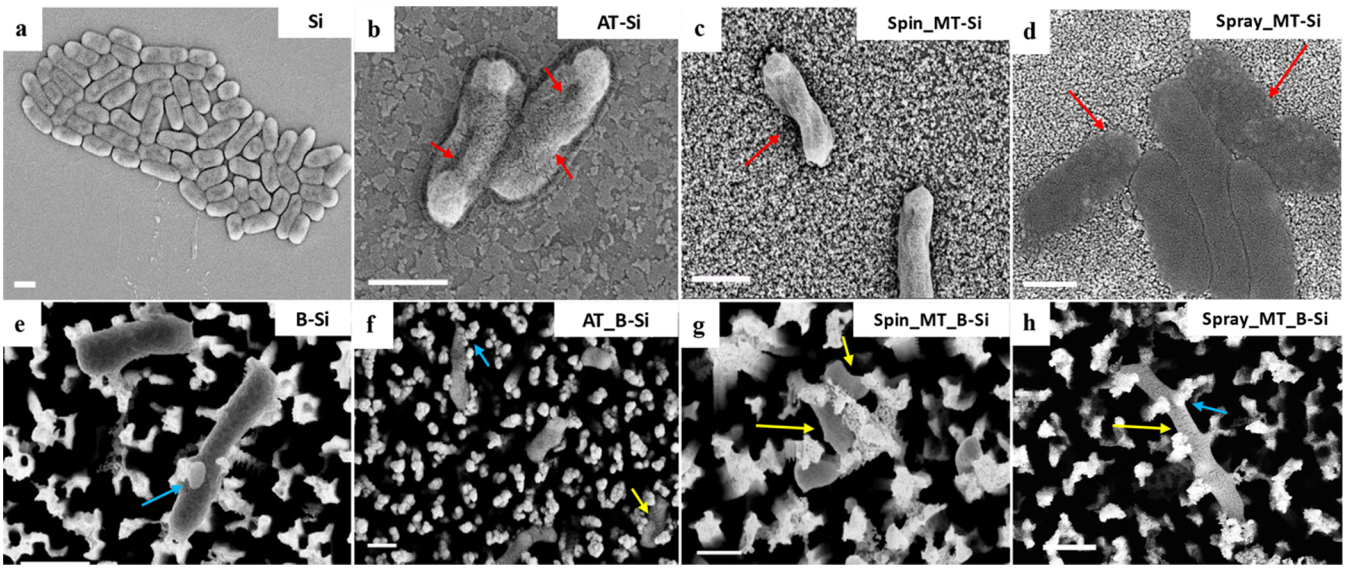

Figure 6. Scanning electron microscopy images of bacteria on different substrates. Blue arrows indicate the piercing of bacteria by pillars. Red arrows indicate cell wall damaged areas. Yellow arrows indicate sunken bacteria. (a) Undamaged bacteria on flat Si. (b–d) Bacterial cell wall disruption on ALD-, spin-, and spray-coated TiO_2 surfaces, respectively. (e) Bacterial cell has been pierced by nanostructures of black Si. (f–h) Bacteria have sunken inside the TiO_2-coated pillars, indicating cell death (Scale bar: 1 μm).

min). Si wafers were further dipped in a 1:50 HF solution to remove the chemical oxide, followed by rinsing in deionized water. The Si wafers were blow-dried with a nitrogen gun and dehydrated on a hot plate at 100 °C for 5 min. These substrates were etched using an optimized recipe for black Si using a modified Bosch process in a deep reactive ion etcher (DRIE). The recipe uses SF_6 and O_2 gases for etching and C_4F_8 gas for passivation to achieve high-aspect-ratio nanopillars on the surface. The fabrication conditions of the etching chamber were as follows: RF, 100 W; pressure, 35 mTorr; back cooling electrode He, 5 Torr; and 36 and 40 sccm (standard cubic centimeter per minute) of O_2 and SF_6 flow, respectively. After fabrication of nanopillars, the sample was cleaned using an O_2 descum recipe to remove the deposited polymer layer on the nanopillars that provided hydrophobicity to the surfaces. This step ensured that the surface would not repel further coatings. After the fabrication of the structured surface, TiO_2 was coated on these structures using three different methods. In the first method, a conformal thin film of 50 nm TiO_2 was deposited using atomic layer deposition (ALD). Second, TiO_2 nanoparticles of 20 nm size and Dyesol(R) 18NR-T titania paste, purchased from Sigma Aldrich, diluted in ethanol in a ratio of 1:4 were spin-coated on the substrates. Third, the same nanoparticles were spray-coated and optimized to the following parameters: the flow rate was fixed to 100 μL/min based on nozzle design and deposition time was 15 s on a substrate preheated to 60 °C. Both spin- and spray-coated samples were subjected to annealing at 500 °C for 1 h to improve the cohesion and adhesion of particles to the substrate. The substrate was preheated to evaporate solvent ethanol, leaving behind only TiO_2 nanoparticles on the pillar. With spin and spray coating, the nanoparticles were nonuniformly distributed in-between and on the highly rough nanostructures.

4.2. Characterization of the Dual Surface. *4.2.1. Scanning Electron Microscopy.* The images of B-Si and TiO_2-coated B-Si were taken using a Carl Zeiss field emission scanning electron microscope, operating at 5 kV. The calculation of the average distance between pillars was performed using ImageJ software. For bacterial sample imaging, substrates were washed twice with phosphate-buffered saline (PBS). The samples were dipped in a solution of 3.5% formaldehyde for 15 min to fix the cells. The solution was serially replaced with 30, 50, 70, 90, and 100% ethanol for the chemical removal of water from the specimen. A 15 nm thin layer of gold was sputtered on the samples using a Quorum sputter coater to avoid the charging effect while performing SEM.

4.2.2. Atomic Force Microscopy. The surface roughness of the substrate was estimated using a Bruker atomic force microscope in ScanAsyst Mode. The images were analyzed with Nanoscope Analysis software V.1.8.

4.2.3. UV Light Source. The bacterial cells on different surfaces were exposed to 19 W/m^2 UVA radiation for 15 min. The light source was a Philips TL-K 40W/10-R UVA lamp. The spectrum of the lamp spans from 315 to 380 nm, with a peak wavelength at 365 nm. The photometric data of the UV source are provided in Figure 4a. UV contained in the air mass (AM) 1.5 solar spectrum is lower than the intensity used for this study and lower than most studies on UV-based photocatalytic layers.[55]

4.2.4. Dye Degradation Measurement. Methylene blue dye was used to quantify the generated ROS. MB is an organic dye that degrades due to ROS produced by TiO_2 in the presence of UV and water. Therefore, its peak absorbance value at 664 nm starts to reduce, using which generated ROS was quantified. Samples of 1 × 1 cm^2 were kept horizontally in glass Petri dishes and submerged in 4 mL of 0.01 mM dye. The samples were kept immersed in MB solution in the dark for 3 h to avoid any adsorption-related transients. They were then exposed to UV light with a wavelength peak at 365 nm for 0–120 min. The distance between the light source and the samples was maintained at 5 cm for all experiments. At an interval of 30 min of UVA exposure, the absorption spectrum of MB was measured using a Shimadzu MPC3600 UV–vis–NIR spectrometer. Wavelengths ranging from 250 to 800 nm were used for reflectance measurement. A D2 light source was used for the range of 250–310 nm, and a tungsten source was used for the

https://doi.org/10.1021/acsomega.1c06706
ACS Omega 2022, 7, 7816–7824

range of 310−800 nm. The equipment used a photomultiplier tube (PMT) detector.

4.2.5. Finite-Difference Time-Domain Simulations. Two types of Si nanostructured arrays with TiO_2 were modeled. The absorption was compared in the smooth versus rough coating of TiO_2 using Ansys Lumerical's finite-difference time-domain (FDTD) simulations. The object "rough wire" used to simulate absorption in the TiO_2 coating was made using multiple rough surfaces that were characterized by an RMS amplitude and correlation length. The rough surface was then wrapped to create a cylindrical shape. The roughness was generated by creating a random matrix of values in K space. A Gaussian filter was applied to this matrix; then, a Fourier transform was used to transform the matrix back to real space. Due to the way the Fourier transform was setup, the roughness would be periodic with period x, y span. This is necessary to avoid a seam when wrapping the rough surface to create a cylindrical shape. The following standard parameters were used to define the roughness of the TiO_2 layer: radius of wire, 0.18; RMS amplitude of roughness, 0.01; correlation length, × 0.01; correlation length z, 0.1; and sampling resolution in the x−y plane, 0.01 um. The wavelength of the simulation light source was 365 nm, which is the peak wavelength of the source used in the experiments, and the intensity of the incident field was defined as 1 unit. The incident light absorbed was calculated using the following equation

$$P_{abs} = -0.5 \text{ w } |E|^2 \text{ imag } (\varepsilon)$$

where ε is the permittivity of the material. This value is integrated over the whole volume of the monitor to obtain the total power absorbed.

4.2.6. Bacterial Growth Conditions and Sample Preparation. Isolated single colonies of *E. coli ATCC 25922* were used to prepare the preinoculum. The culture was grown for 12 h in Luria Broth (LB) medium at 37 °C with constant shaking at 120 rpm. Fifty microliters of the preinoculum was added to 10 mL of LB and was allowed to grow until 0.8 OD (optical density) at 600 nm. The cells were subsequently pelleted and washed with PBS. A cell suspension of 0.8 OD at 600 nm was used for performing the experiments.

4.2.7. Bacteria Viability Assay. The bacterial strain of *E. coli ATCC 25922* was used to evaluate the antibacterial activity of the surfaces. The cells were cultivated in Luria-Bertani broth from a single colony and incubated overnight at 37 °C. Two milliliters of the overnight grown bacterial culture (0.8 optical density) was centrifuged, and the supernatant was removed. It was then resuspended in an equal volume of 0.9% saline. Next, 20 μL of saline-suspended bacteria were added to the substrates; the substrates placed in the well plate were immersed in a water-cooled jacket to prevent temperature elevation and exposed to UVA (365 nm) light with an intensity of 19 W/m^2 for 15 min. The substrates were immersed in a 1 mL saline solution contained in 50 mL centrifuge tubes. The bacteria were separated from the surface by gentle retropipetting. Further, the bacteria were serially diluted and mixed thoroughly using retropipetting. Five microliters of the suspensions were plated on nutrient agar plates. The plates were incubated overnight for bacterial colonies to grow at 37 °C. The number of colonies grown was counted and multiplied by the appropriate dilution factor to determine the number of CFU/mL in the original sample. Experiments were repeated thrice, and the normalized CFU/mL was calculated.

AUTHOR INFORMATION

Corresponding Author

Jagriti Singh − *Centre for Nanoscience and Engineering, Indian Institute of Science, Bengaluru 560012, India;* orcid.org/0000-0003-1164-1375; Email: jagriti@iisc.ac.in

Authors

Prajwal B. Hegde − *Centre for Nanoscience and Engineering, Indian Institute of Science, Bengaluru 560012, India*

Sushobhan Avasthi − *Centre for Nanoscience and Engineering, Indian Institute of Science, Bengaluru 560012, India;* orcid.org/0000-0001-6201-7711

Prosenjit Sen − *Centre for Nanoscience and Engineering, Indian Institute of Science, Bengaluru 560012, India;* orcid.org/0000-0001-6519-1707

Complete contact information is available at: https://pubs.acs.org/10.1021/acsomega.1c06706

Author Contributions

The manuscript was written through the contributions of all authors. All authors have given approval to the final version of the manuscript.

Notes

The authors declare no competing financial interest.

ACKNOWLEDGMENTS

The authors would like to acknowledge the usage of the facilities at the National Nanofabrication Centre (NNFC, CeNSE) and the Micro/Nano Characterization Facility (MNCF, CeNSE) at IISc for the fabrication and characterization work done. The authors acknowledge funding support from MHRD, MeitY, and DST Nano Mission. The authors also acknowledge Shubham Jadhav and Radhanshu Sharma for their help in carrying out the experiments.

REFERENCES

(1) Sugden, R.; Kelly, R.; Davies, S. Combatting Antimicrobial Resistance Globally. *Nat. Microbiol.* **2016**, *1*, No. 16187.

(2) Burki, T. K. Superbugs: An Arms Race Against Bacteria. *Lancet Respir. Med.* **2018**, *6*, 668.

(3) Roope, L. S. J.; Smith, R. D.; Pouwels, K. B.; Buchanan, J.; Abel, L.; Eibich, P.; Butler, C. C.; Tan, P. S.; Sarah Walker, A.; Robotham, J. V.; Wordsworth, S. The Challenge of Antimicrobial Resistance: What Economics Can Contribute. *Science* **2019**, *364*, No. eaau4679.

(4) Dadgostar, P. Antimicrobial Resistance: Implications and Costs. *Infect. Drug Resist.* **2019**, *12*, 3903−3910.

(5) Russotto, V.; Cortegiani, A.; Raineri, S. M.; Giarratano, A. Bacterial Contamination of Inanimate Surfaces and Equipment in the Intensive Care Unit. *J. Intensive Care* **2015**, *3*, No. 54.

(6) Yasuyuki, M.; Kunihiro, K.; Kurissery, S.; Kanavillil, N.; Sato, Y.; Kikuchi, Y. Antibacterial Properties of Nine Pure Metals: A Laboratory Study Using Staphylococcus Aureus and *Escherichia Coli*. *Biofouling* **2010**, *26*, 851−858.

(7) Vaidya, M. Y.; McBain, A. J.; Butler, J. A.; Banks, C. E.; Whitehead, K. A. Antimicrobial Efficacy and Synergy of Metal Ions against Enterococcus Faecium, Klebsiella Pneumoniae and Acinetobacter Baumannii in Planktonic and Biofilm Phenotypes. *Sci. Rep.* **2017**, *7*, No. 5911.

(8) Slavin, Y. N.; Asnis, J.; Häfeli, U. O.; Bach, H. Metal Nanoparticles: Understanding the Mechanisms behind Antibacterial Activity. *J. Nanobiotechnol.* **2017**, *15*, 1−20.

(9) Domb, A. J.; Yudovin-Farber, I.; Golenser, J.; Beyth, N.; Weiss, E. I. Quaternary Ammonium Polyethyleneimine: Antibacterial Activity. *J. Nanomater.* **2010**, *2010*, No. 826343.

https://doi.org/10.1021/acsomega.1c06706
ACS Omega 2022, 7, 7816−7824

(10) Hassan, E. A.; Hassan, M. L.; Abou-zeid, R. E.; El-Wakil, N. A. Novel Nanofibrillated Cellulose/Chitosan Nanoparticles Nanocomposites Films and Their Use for Paper Coating. *Ind. Crops Prod.* **2016**, *93*, 219−226.
(11) Robertson, J.; Gizdavic-Nikolaidis, M.; Swift, S. Investigation of Polyaniline and a Functionalised Derivative as Antimicrobial Additives to Create Contamination Resistant Surfaces. *Materials* **2018**, *11*, No. 436.
(12) Sanchez Ramirez, D. O.; Varesano, A.; Carletto, R. A.; Vineis, C.; Perelshtein, I.; Natan, M.; Perkas, N.; Banin, E.; Gedanken, A. Antibacterial Properties of Polypyrrole-Treated Fabrics by Ultrasound Deposition. *Mater. Sci. Eng., C* **2019**, *102*, 164−170.
(13) Saidin, S.; Jumat, M. A.; Mohd Amin, N. A. A.; Saleh Al-Hammadi, A. S. Organic and Inorganic Antibacterial Approaches in Combating Bacterial Infection for Biomedical Application. *Mater. Sci. Eng., C* **2021**, *118*, No. 111382.
(14) Yousefi, M.; Dadashpour, M.; Hejazi, M.; Hasanzadeh, M.; Behnam, B.; de la Guardia, M.; Shadjou, N.; Mokhtarzadeh, A. Anti-Bacterial Activity of Graphene Oxide as a New Weapon Nanomaterial to Combat Multidrug-Resistance Bacteria. *Mater. Sci. Eng., C* **2017**, *74*, 568−581.
(15) Gutiérrez, B.; J, M.; Conceição, K.; de Andrade, V. M.; Trava-Airoldi, V. J.; Capote, G. High Antibacterial Properties of DLC Film Doped with Nanodiamond. *Surf. Coat. Technol.* **2019**, *375*, 395−401.
(16) Skariyachan, S.; Parveen, A.; Garka, S. Nanoparticle Fullerene (C60) Demonstrated Stable Binding with Antibacterial Potential towards Probable Targets of Drug Resistant Salmonella Typhi - a Computational Perspective and in Vitro Investigation. *J. Biomol. Struct. Dyn.* **2017**, *35*, 3449−3468.
(17) Cui, H.; Gu, Z.; Chen, X.; Lin, L.; Wang, Z.; Dai, X.; Yang, Z.; Liu, L.; Zhou, R.; Dong, M. Stimulating Antibacterial Activities of Graphitic Carbon Nitride Nanosheets with Plasma Treatment. *Nanoscale* **2019**, *11*, 18416−18425.
(18) Qiao, Y.; Liu, X.; Li, B.; Han, Y.; Zheng, Y.; Yeung, K. W. K.; Li, C.; Cui, Z.; Liang, Y.; Li, Z.; Zhu, S.; Wang, X.; Wu, S. Treatment of MRSA-Infected Osteomyelitis Using Bacterial Capturing, Magnetically Targeted Composites with Microwave-Assisted Bacterial Killing. *Nat. Commun.* **2020**, *11*, No. 1905185.
(19) Guan, W.; Tan, L.; Liu, X.; Cui, Z.; Zheng, Y.; Yeung, K. W. K.; Zheng, D.; Liang, Y.; Li, Z.; Zhu, S.; Wang, X.; Wu, S. Ultrasonic Interfacial Engineering of Red Phosphorous−Metal for Eradicating MRSA Infection Effectively. *Adv. Mater.* **2021**, *33*, No. 2006047.
(20) Zhou, Z.; Li, B.; Liu, X.; Li, Z.; Zhu, S.; Liang, Y.; Cui, Z.; Wu, S. Recent Progress in Photocatalytic Antibacterial. *ACS Appl. Bio Mater.* **2021**, *4*, 3909−3936.
(21) Xu, J. W.; Yao, K.; Xu, Z. K. Nanomaterials with a Photothermal Effect for Antibacterial Activities: An Overview. *Nanoscale* **2019**, *11*, 8680−8691.
(22) Mao, C.; Xiang, Y.; Liu, X.; Cui, Z.; Yang, X.; Li, Z.; Zhu, S.; Zheng, Y.; Yeung, K. W. K.; Wu, S. Repeatable Photodynamic Therapy with Triggered Signaling Pathways of Fibroblast Cell Proliferation and Differentiation to Promote Bacteria-Accompanied Wound Healing. *ACS Nano* **2018**, *12*, 1747−1759.
(23) Luttrell, T.; Halpegamage, S.; Tao, J.; Kramer, A.; Sutter, E.; Batzill, M. Why Is Anatase a Better Photocatalyst than Rutile? - Model Studies on Epitaxial TiO2 Films. *Sci. Rep.* **2015**, *4*, No. 4043.
(24) Sun, L.; Bolton, J. R. Determination of the Quantum Yield for the Photochemical Generation of Hydroxyl Radicals in TiO2 Suspensions. *J. Phys. Chem. A* **1996**, *100*, 4127−4134.
(25) Ivanova, E. P.; Linklater, D. P.; Werner, M.; Baulin, V. A.; Xu, X. M.; Vrancken, N.; Rubanov, S.; Hanssen, E.; Wandiyanto, J.; Truong, V. K.; Elbourne, A.; Maclaughlin, S.; Juodkazis, S.; Crawford, R. J. The Multi-Faceted Mechano-Bactericidal Mechanism of Nanostructured Surfaces. *Proc. Natl. Acad. Sci. U.S.A.* **2020**, *117*, 12598−12605.
(26) Kim, S.; Jung, U. T.; Kim, S. K.; Lee, J. H.; Choi, H. S.; Kim, C. S.; Jeong, M. Y. Nanostructured Multifunctional Surface with Antireflective and Antimicrobial Characteristics. *ACS Appl. Mater. Interfaces* **2015**, *7*, 326−331.
(27) Valle, J.; Burgui, S.; Langheinrich, D.; Gil, C.; Solano, C.; Toledo-Arana, A.; Helbig, R.; Lasagni, A.; Lasa, I. Evaluation of Surface Microtopography Engineered by Direct Laser Interference for Bacterial Anti-Biofouling. *Macromol. Biosci.* **2015**, *15*, 1060−1069.
(28) Serrano, C.; García-Fernández, L.; Fernández-Blázquez, J. P.; Barbeck, M.; Ghanaati, S.; Unger, R.; Kirkpatrick, J.; Arzt, E.; Funk, L.; Turón, P.; del Campo, A. Nanostructured Medical Sutures with Antibacterial Properties. *Biomaterials* **2015**, *52*, 291−300.
(29) Ali, M.; Zhou, F.; Chen, K.; Kotzur, C.; Xiao, C.; Bourgeois, L.; Zhang, X.; MacFarlane, D. R. Nanostructured Photoelectrochemical Solar Cell for Nitrogen Reduction Using Plasmon-Enhanced Black Silicon. *Nat. Commun.* **2016**, *7*, No. 11335.
(30) Hasan, J.; Jain, S.; Chatterjee, K. Nanoscale Topography on Black Titanium Imparts Multi-Biofunctional Properties for Orthopedic Applications. *Sci. Rep.* **2017**, *7*, No. 41118.
(31) Xie, X.; Mao, C.; Liu, X.; Tan, L.; Cui, Z.; Yang, X.; Zhu, S.; Li, Z.; Yuan, X.; Zheng, Y.; Yeung, K. W. K.; Chu, P. K.; Wu, S. Tuning the Bandgap of Photo-Sensitive Polydopamine/Ag3PO4/Graphene Oxide Coating for Rapid, Noninvasive Disinfection of Implants. *ACS Cent. Sci.* **2018**, *4*, 724−738.
(32) Lv, R.; Liang, Y. Q.; Li, Z. Y.; Zhu, S. L.; Cui, Z. D.; Wu, S. L. Flower-like CuS/Graphene Oxide with Photothermal and Enhanced Photocatalytic Effect for Rapid Bacteria-Killing Using Visible Light. *Rare Met.* **2021**, DOI: 10.1007/s12598-021-01759-4.
(33) Han, D.; Li, Y.; Liu, X.; Li, B.; Han, Y.; Zheng, Y.; Yeung, K. W. K.; Li, C.; Cui, Z.; Liang, Y.; Li, Z.; Zhu, S.; Wang, X.; Wu, S. Rapid Bacteria Trapping and Killing of Metal-Organic Frameworks Strengthened Photo-Responsive Hydrogel for Rapid Tissue Repair of Bacterial Infected Wounds. *Chem. Eng. J.* **2020**, *396*, No. 125194.
(34) Luo, Y.; Liu, X.; Tan, L.; Li, Z.; Yeung, K. W. K.; Zheng, Y.; Cui, Z.; Liang, Y.; Zhu, S.; Li, C.; Wang, X.; Wu, S. Enhanced Photocatalytic and Photothermal Properties of Ecofriendly Metal-Organic Framework Heterojunction for Rapid Sterilization. *Chem. Eng. J.* **2021**, *405*, No. 126730.
(35) Huang, B.; Tan, L.; Liu, X.; Li, J.; Wu, S. A Facile Fabrication of Novel Stuff with Antibacterial Property and Osteogenic Promotion Utilizing Red Phosphorus and Near-Infrared Light. *Bioact. Mater.* **2019**, *4*, 17−21.
(36) Tan, L.; Li, J.; Liu, X.; Cui, Z.; Yang, X.; Zhu, S.; Li, Z.; Yuan, X.; Zheng, Y.; Yeung, K. W. K.; Pan, H.; Wang, X.; Wu, S. Rapid Biofilm Eradication on Bone Implants Using Red Phosphorus and Near-Infrared Light. *Adv. Mater.* **2018**, *30*, No. 1801808.
(37) Mao, C.; Xiang, Y.; Liu, X.; Cui, Z.; Yang, X.; Yeung, K. W. K.; Pan, H.; Wang, X.; Chu, P. K.; Wu, S. Photo-Inspired Antibacterial Activity and Wound Healing Acceleration by Hydrogel Embedded with Ag/Ag@AgCl/ZnO Nanostructures. *ACS Nano* **2017**, *11*, 9010−9021.
(38) Xiang, Y.; Zhou, Q.; Li, Z.; Cui, Z.; Liu, X.; Liang, Y.; Zhu, S.; Zheng, Y.; Yeung, K. W. K.; Wu, S. A Z-Scheme Heterojunction of ZnO/CDots/C3N4 for Strengthened Photoresponsive Bacteria-Killing and Acceleration of Wound Healing. *J. Mater. Sci. Technol.* **2020**, *57*, 1−11.
(39) Su, K.; Tan, L.; Liu, X.; Cui, Z.; Zheng, Y.; Li, B.; Han, Y.; Li, Z.; Zhu, S.; Liang, Y.; Feng, X.; Wang, X.; Wu, S. Rapid Photo-Sonotherapy for Clinical Treatment of Bacterial Infected Bone Implants by Creating Oxygen Deficiency Using Sulfur Doping. *ACS Nano* **2020**, *14*, 2077−2089.
(40) Singh, J.; Jadhav, S.; Avasthi, S.; Sen, P. Designing Photocatalytic Nanostructured Antibacterial Surfaces: Why Is Black Silica Better than Black Silicon? *ACS Appl. Mater. Interfaces* **2020**, *12*, 20202.
(41) Percin, D.; Sav, H.; Hormet-Oz, H. T.; Karauz, M. The Relationship Between Holding Time and the Bacterial Load on Surgical Instruments. *Indian J. Surg.* **2015**, *77*, 16−18.
(42) Man, N. K.; Degremont, A.; Darbord, J. C.; Collet, M.; Vaillant, P. Evidence of Bacterial Biofilm in Tubing from Hydraulic Pathway of Hemodialysis System. *Artif. Organs* **1998**, *22*, 596−600.
(43) Lopez-Lopez, G.; Pascual, A.; Perea, E. J. Effect of Plastic Catheter Material on Bacterial Adherence and Viability. *J. Med. Microbiol.* **1991**, *34*, 349−353.

https://doi.org/10.1021/acsomega.1c06706
ACS Omega 2022, 7, 7816−7824

(44) Wojgani, H.; Kehsa, C.; Cloutman-Green, E.; Gray, C.; Gant, V.; Klein, N. Hospital Door Handle Design and Their Contamination with Bacteria: A Real Life Observational Study. Are We Pulling against Closed Doors? *PLoS One* **2012**, *7*, No. e40171.
(45) Huslage, K.; Rutala, W. A.; Sickbert-Bennett, E.; Weber, D. J. A Quantitative Approach to Defining "High-Touch" Surfaces in Hospitals. *Infect. Control Hosp. Epidemiol.* **2010**, *31*, 850−853.
(46) Creighton, J. R.; Ho, P. Chapter 1 Introduction to Chemical Vapor Deposition (CVD). *Chem. Vap. Deposition* **2001**, 1−13.
(47) Oviroh, P. O.; Akbarzadeh, R.; Pan, D.; Coetzee, R. A. M.; Jen, T. C. New Development of Atomic Layer Deposition: Processes, Methods and Applications. *Sci. Technol. Adv. Mater.* **2019**, *20*, 465−496.
(48) Pichat, P. *Photocatalytic Coatings*; Elsevier, 2014; Vol. *4*.
(49) Tripathy, A.; Kumar, A.; Sreedharan, S.; Muralidharan, G.; Pramanik, A.; Nandi, D.; Sen, P. Fabrication of Low-Cost Flexible Superhydrophobic Antibacterial Surface with Dual-Scale Roughness. *ACS Biomater. Sci. Eng.* **2018**, *4*, 2213−2223.
(50) Ge, X.; Zhao, J.; Esmeryan, K. D.; Lu, X.; Li, Z.; Wang, K.; Ren, F.; Wang, Q.; Wang, M.; Qian, B. Cicada-Inspired Fluoridated Hydroxyapatite Nanostructured Surfaces Synthesized by Electrochemical Additive Manufacturing. *Mater. Des.* **2020**, *193*, No. 108790.
(51) Lee, K. G.; Choi, B. G.; Kim, B., Il; Shyu, T.; Oh, M. S.; Im, S. G.; Chang, S. J.; Lee, T. J.; Kotov, N. A.; Lee, S. J. Scalable Nanopillar Arrays with Layer-by-Layer Patterned Overt and Covert Images. *Adv. Mater.* **2014**, *26*, 6119−6124.
(52) Hui, R.; Wang, Z.; Yick, S.; Maric, R.; Ghosh, D. Fabrication of Ceramic Films for Solid Oxide Fuel Cells via Slurry Spin Coating Technique. *J. Power Sources* **2007**, *172*, 840−844.
(53) Perednis, D.; Gauckler, L. J. Thin Film Deposition Using Spray Pyrolysis. *J. Electroceram.* **2005**, *14*, 103−111.
(54) Tripathy, A.; Sen, P.; Su, B.; Briscoe, W. H. Natural and Bioinspired Nanostructured Bactericidal Surfaces. *Adv. Colloid Interface Sci.* **2017**, *248*, 85−104.
(55) Joost, U.; Juganson, K.; Visnapuu, M.; Mortimer, M.; Kahru, A.; Nõmmiste, E.; Joost, U.; Kisand, V.; Ivask, A. Photocatalytic Antibacterial Activity of Nano-TiO2 (Anatase)-Based Thin Films: Effects on *Escherichia Coli* Cells and Fatty Acids. *J. Photochem. Photobiol., B* **2015**, *142*, 178−185.

https://doi.org/10.1021/acsomega.1c06706
ACS Omega 2022, 7, 7816−7824